

# **SANDIA REPORT**

SAND2014-18346

Unlimited Release

Printed October 2014

## **Bistatic SAR: Imagery & Image Products**

David A. Yocky, Daniel E. Wahl, and Charles V. Jakowatz, Jr.

Prepared by  
Sandia National Laboratories  
Albuquerque, New Mexico 87185 and Livermore, California 94550

Sandia National Laboratories is a multi-program laboratory managed and operated by Sandia Corporation, a wholly owned subsidiary of Lockheed Martin Corporation, for the U.S. Department of Energy's National Nuclear Security Administration under contract DE-AC04-94AL85000.

Approved for public release; further dissemination unlimited.



**Sandia National Laboratories**

Issued by Sandia National Laboratories, operated for the United States Department of Energy by Sandia Corporation.

**NOTICE:** This report was prepared as an account of work sponsored by an agency of the United States Government. Neither the United States Government, nor any agency thereof, nor any of their employees, nor any of their contractors, subcontractors, or their employees, make any warranty, express or implied, or assume any legal liability or responsibility for the accuracy, completeness, or usefulness of any information, apparatus, product, or process disclosed, or represent that its use would not infringe privately owned rights. Reference herein to any specific commercial product, process, or service by trade name, trademark, manufacturer, or otherwise, does not necessarily constitute or imply its endorsement, recommendation, or favoring by the United States Government, any agency thereof, or any of their contractors or subcontractors. The views and opinions expressed herein do not necessarily state or reflect those of the United States Government, any agency thereof, or any of their contractors.

Printed in the United States of America. This report has been reproduced directly from the best available copy.

Available to DOE and DOE contractors from

U.S. Department of Energy  
Office of Scientific and Technical Information  
P.O. Box 62  
Oak Ridge, TN 37831

Telephone: (865) 576-8401  
Facsimile: (865) 576-5728  
E-Mail: [reports@adonis.osti.gov](mailto:reports@adonis.osti.gov)  
Online ordering: <http://www.osti.gov/bridge>

Available to the public from

U.S. Department of Commerce  
National Technical Information Service  
5285 Port Royal Rd.  
Springfield, VA 22161

Telephone: (800) 553-6847  
Facsimile: (703) 605-6900  
E-Mail: [orders@ntis.fedworld.gov](mailto:orders@ntis.fedworld.gov)  
Online order: <http://www.ntis.gov/help/ordermethods.asp?loc=7-4-0#online>



SAND2014-18346  
Unlimited Release  
Printed October 2014

# **Bistatic SAR: Imagery & Image Products**

David A. Yocky, Daniel E. Wahl, and Charles V. Jakowatz, Jr.  
Signal & Image Processing Technologies

Sandia National Laboratories  
P.O. Box 5800  
Albuquerque, New Mexico 87185-MS1207

## **Abstract**

While typical SAR imaging employs a co-located (monostatic) RADAR transmitter and receiver, bistatic SAR imaging separates the transmitter and receiver locations. The transmitter and receiver geometry determines if the scattered signal is back scatter, forward scatter, or side scatter. The monostatic SAR image is backscatter. Therefore, depending on the transmitter/receiver collection geometry, the captured imagery may be quite different than that sensed at the monostatic SAR. This document presents imagery and image products formed from captured signals during the validation stage of the bistatic SAR research. Image quality and image characteristics are discussed first. Then image products such as two-color multi-view (2CMV) and coherent change detection (CCD) are presented.

## **ACKNOWLEDGMENTS**

This work would not have been possible without the support of many people from several organizations. The authors wish to express their gratitude to the National Nuclear Security Administration, Defense Nuclear Nonproliferation Research and Development (DNN R&D). Our team would like to thank our program leader, Veraun Chipman from NSTec for his help and support of our efforts. This work was done by Sandia National Laboratories under award number DE-AC52-06NA25

We would like to thank Paul Eichel (Sandian, retired) for writing and maintaining the image formation, registration, and geo-location computer codes used in this research. We also thank other Bistatic SAR team members: Neall Doren, Terry Bacon, and Bert Tise for their advice and insight on this project. Also, thanks to Cathy Snelson-Gerlicher formerly of NSTec, now at Los Alamos National Laboratory, for supporting our efforts.



# CONTENTS

1.	Introduction .....	7
2.	Bistatic SAR Experiment Sites .....	7
2.1	Manzano Mountain .....	8
2.2	Source Physics Experiment Overlook .....	8
2.3	SAR Illuminators .....	12
2.3.1	COSMO-SkyMed .....	12
2.3.2	TerraSAR-X .....	12
2.4	SAR Collections .....	12
3.	Bistatic SAR Imagery .....	13
3.1	Image formation .....	14
3.2	Bistatic Images .....	14
3.2.1	CSK: June 10, 2013 .....	14
3.2.2	TSX: August 1, 2013 .....	20
3.2.3	CSK: SPE Overlook, August 15, 2013 .....	23
3.3	Image quality .....	27
4.	Bistatic Image Products .....	29
4.1	Two-Color Multi-View .....	29
4.2	Coherent Change Detection .....	29
5.	Conclusions .....	37
	References .....	37
	Distribution .....	39

## FIGURES

Figure 1: Google Earth® optical image of Manzano Mountain and Tijeras Arroyo Golf Course on Kirtland AFB. ....	9
Figure 2: Manzano Mountain antennas set up. The direct-energy antenna is in the background. The reflected-energy antenna is in the foreground. ....	10
Figure 3: Looking down the reflected antenna toward the TAGC in the distance. The small rectangle aluminum object with two circles to the left of the horn antenna is the inclinometer. The yellow object on the tripod is a compass for azimuth pointing. ....	10
Figure 4: Google Earth® optical imagery of the SPE and its overlook. ....	11
Figure 5: SPE overlook site where the base-station is inside the van on the left-side of the picture. The SPE site is the bare-earth patch in the upper right-side of the picture just to the right of the yellow drilling structure from a distant-past experiment. ....	11
Figure 6: Radar coordinates bistatic SAR image of the TAGC from Manzano Mountain on June 10, 2013, 18:46:10 MDT. ....	16
Figure 7: Close-up of the TAGC. Note the roads are curved due to wavefront curvature using PFA. ....	17
Figure 8: Geo-located bistatic SAR image of TAGC captured on June 10, 2013. This image is on a latitude/longitude grid. ....	18
Figure 9: The image on the left is the bistatic SAR, geo-located image of TAGC. The image on the right is the monostatic CSK SAR image from the commercial imagery vender. Note the differences in shadows. The bistatic elevation angle is about $5.6^{\circ}$ and the monostatic elevation is $42.8^{\circ}$ , making the bistatic shadows more pronounced. The target reflectance are quite different in some cases. ....	19
Figure 10: Close-up of the CSK June 10, 2013 TAGC bistatic imagery. Here the glint off the power lines that exist along the golf course is seen as well as the faint return-energy antenna sidelobe inside the red lines. The tree canopy motion defocus because of wind is apparent. ....	20
Figure 11: TSX Bistatic image of TAGC captured on August 1, 2013, 07:15:52 MDT. Image created using PFA. ....	21
Figure 12: Geo-located TSX bistatic SAR imagery captured August 1, 2013 from Manzano Mountain. ....	21
Figure 13: The left image is a close up of TAGC from the geo-located bistatic TSX SAR imagery. The right image is a close up of TAGC from the geo-located monostatic TSX SAR image. ....	22
Figure 14: Bistatic SAR image created using PFA of the SPE site and its surrounding area. ....	24
Figure 15: Geo-located bistatic SAR image of the SPE site and its surroundings. The SPE site and Sedan crater are called-out in the image. ....	25
Figure 16: The left image is the bistatic image formed from captured CSK signals on August 15, 2013 at 18:46:10 PDT of the SPE pad and surrounding area. The elevation angle of the reflect-energy antenna was $5.5^{\circ}$ . The yellow lines delineate receiver shadows. The red circle encloses the SPE pad. The right image is the monostatic CSK image. The green arrow denotes the direction of illumination. The yellow arrows show possible areas of layover. The information about the	

mountain slopes here are virtually lost and distorted in the SAR range direction. The SPE pad and the road to it are darker in the monostatic than the bistatic image. ....	26
Figure 17: Image distortions in SAR imagery. Layover occurs when a target of height, i.e., a mountain appears in the same range as a lower height target, i.e. a valley. Foreshortening occurs when sloped sides of a mountain are contracted in size because of slope and height of the mountain. ....	27
Figure 18: Two-color multi-view (2CMV) of June 10, 2013 (red) and June 11, 2013 (green & blue) TAGC bistatic imagery. The overall background is grayish meaning there is no change. Yet there are small vehicle differences in the TAGC parking lot. There are changes of the glint off the power lines on the left of the image and tree structures at the top of the image. ....	32
Figure 19: The 2CMV of June 11, 2013 (red) and June 14, 2013 (green & blue) bistatic imagery at TAGC. Here the intensity of June 11 is a little higher giving the overall reddish hue of the image. Notable changes are blue vehicles in the golf course parking lot and blue glint off the power lines. Other changes include red and blue changes in the tree structure, and three vehicles “fled” near the right-middle of the image. ....	33
Figure 20: The left-most figure is the CSK June 10, 2013 bistatic, geo-located image of TAGC. The right-most figure is the coherent change detection (CCD) of the CSK June 10, 2013 and June 11, 2013. White pixels are high-valued complex correlation. CCD is dependent on the two images signal-to-noise, so the targets closer to the receive-energy antenna on the right-side of both images, can be higher correlated if no temporal change has occurred between collected images. Also, targets farther from the receive antenna will have inherently lower signal-to-noise, thus lower complex correlation/CCD value. ....	34
Figure 21: The left-most image is a close-up of the TAGC area of June 10, 2013 CSK bistatic imagery. The right-most image is the CCD between June 10, 2013 and June 11, 2013. Note the smeared tree canopies in the image also show as decorrelation (low values) in the CCD. The sidelobe that is barely visible in the image decorrelates in the CCD. Areas of low returns such as shadows are also decorrelated in the CCD. ....	35

## TABLES

Table 1: Table of commercial SAR collections for the field experiments. ....	13
Table 2: Table of coherent CSK collections over Kirtland AFB with bistatic collection geometry angles. ....	31

## NOMENCLATURE

2CMV	two-color multi-view
AFB	Air Force Base
CCD	coherent change detection
CSK	COSMO-SkyMed
dB	decibel
ESA	electronically-steered array
Hz	Hertz
LEO	low earth orbit
MDT	Mountain Daylight Time
NNSS	Nevada National Security Site
NSTec	National Securities Technologies
PDT	Pacific Daylight Time
PFA	polar format algorithm
RADAR	radio detection and ranging
RF	radio frequency
SAR	synthetic aperture RADAR
SNL	Sandia National Laboratories
SNR	signal-to-noise ratio
SPE	Source Physics Experiment
TAGC	Tijeras Arroyo Golf Course
TLE	two-line element
TSX	TerraSAR-X



## **1. INTRODUCTION**

The National Center for Nuclear Security (NCNS) has funded Sandia National Laboratories (SNL) to explore the feasibility of deploying a ground-based radio detection and ranging (RADAR) signal receiver coupled with the capability of recording and digitizing the collected signal. The motivation for this research stems from the desire to passively capture irradiating synthetic aperture RADAR (SAR) signals. If the transmitted and reflected signals are captured from the illuminating SAR, SNL proposes the possibility of creating an image of targets the illuminating SAR observes. The proof of concept and the signal processing for image formation has been presented [1, 2].

While typical SAR imaging employs a co-located (monostatic) RADAR transmitter and receiver, bistatic SAR imaging separates the transmitter and receiver locations. The transmitter and receiver geometry determines if the scattered signal is back scatter, forward scatter, or side scatter. The monostatic SAR image is backscatter. Therefore, depending on the transmitter/receiver collection geometry, the captured imagery may be quite different that that sensed at the monostatic SAR.

This document presents imagery and image products formed from captured signals during the validation stage of the bistatic SAR research. Image quality and image characteristics are discussed first. Then image products such as two-color multi-view (2CMV) and coherent change detection (CCD) are presented.

## **2. BISTATIC SAR EXPERIMENT SITES**

While typical SAR imaging employs a co-located RADAR transmitter and receiver, bistatic SAR imaging separates the transmitter and receiver locations. A bistatic SAR configuration allows for the transmitter and receiver(s) to be in a variety of geometric alignments. For example, if the transmitter illuminates the ground from behind the receiver position, the scattered signal from the target is captured as it travels back, toward the receiver's position. This is called backscatter. If the transmitter illuminates the ground from a location in front of the receiver, the scattering signal is called "forward scatter". Side scattering positions fill the rest of possible collection geometries.

SNL proposes the deployment of a ground-based RADAR receiver. If this RADAR receiver is coupled with the capability of digitizing and recording the signal collected, one could capture SAR radiation illuminating targets of interest. The irradiating SAR would not know the ground-based receiver's location, thus the SAR signal is passively and covertly captured. If the transmitted and reflected signals are captured from the illuminating SAR, SNL proposes the possibility of creating an image of targets the illuminating SAR observes.

The bistatic RADAR receiving system consists of two RADAR receivers (horn antennas). The first receiver will be pointed skyward to capture the direct signal from the illuminating RADAR. The second receiver will be directed toward the ground region of interest to capture the targets illuminated by the transmitting RADAR. These RADAR signals will be captured by the antennas, digitized by hardware, and stored on a hard drive for later analysis and image formation.

This document describes the developed hardware, software, bistatic SAR configuration, and its deployment to test the concept of a ground-based bistatic SAR. In the proof-of-concept experiments herein, the RADAR transmitter will be a commercial SAR satellite and the RADAR receiver will be deployed at ground level, observing and capturing RADAR ground/targets illuminated by the satellite system.

## **2.1 Manzano Mountain**

Manzano Mountain on Kirtland AFB provides a large relief above the plains that gradually slope to the Rio Grande. Figure 1 shows a Google Earth® image of Kirtland AFB with a pin icon at the deployment site on Manzano Mountain and the target, Tijeras Arroyo Golf Course (TAGC) and its club house. The deployment point is at  $35^{\circ} 01' 22.9''$  N,  $106^{\circ} 29' 14.8''$  W with a relief of 340 m and a stand-off distance of 3.68 km from TAGC. CSK and TSX can illuminate from east-to-west in a descending orbital pass, or from west-to-east in an ascending orbital pass. Manzano Mountain offers backscatter (descending orbit) and forward-scatter (ascending orbit) bistatic capture geometries. Backscatter geometry will produce an image closest to the monostatic SAR image sensed by the illuminator.

Figure 2 shows the deployment of the direct-energy antenna, in the background pointed to the sky, and the reflected-energy antenna, next to the Sandian. Figure 3 displays the view from the reflected-energy antenna toward the TAGC.

## **2.2 Source Physics Experiment Overlook**

A flat drill pad has been created at  $37^{\circ} 13' 16.8''$  N,  $116^{\circ} 03' 38.8''$  W at NNSS. At this site, three underground conventional explosive tests have been conducted under the NCNS project called Source Physics Experiment (SPE). The site is instrumented to monitor seismic, acoustic, and other signals pertinent to characterizing the explosions. The site is in the foothills at the north-most extent of Yucca Flat. It is surrounded by mountainous terrain to the east, north, and west.

To the north-northeast of the SPE pad, an unmaintained mining road rises to an overlook of the SPE site. It is approximately 1530 m away with a relief of 160 m above the SPE site at coordinates  $37^{\circ} 14' 03.6''$  N,  $116^{\circ} 03' 22.6''$  W. This overlook provides a side-scattering

geometry for bistatic signal collection, but it was the only site that gave relief above the SPE site, a good stand-off distance, and line-of-site to monitor SPE activities. Also, commercial SAR imagery was permitted to be collected over the SPE site. Figure 4 shows a Google Earth® optical image of SPE and the overlook. Figure 5 shows the deployment of the van containing the base station and two tripods holding the bistatic antennas.



**Figure 1: Google Earth® optical image of Manzano Mountain and Tijeras Arroyo Golf Course on Kirtland AFB.**





**Figure 2: Manzano Mountain antennas set up. The direct-energy antenna is in the background. The reflected-energy antenna is in the foreground.**



**Figure 3: Looking down the reflected antenna toward the TAGC in the distance. The small rectangle aluminum object with two circles to the left of the horn antenna is the inclinometer. The yellow object on the tripod is a compass for azimuth pointing.**



**Figure 4: Google Earth® optical imagery of the SPE and its overlook.**



**Figure 5: SPE overlook site where the base-station is inside the van on the left-side of the picture. The SPE site is the bare-earth patch in the upper right-side of the picture just to the right of the yellow drilling structure from a distant-past experiment.**

## **2.3 SAR Illuminators**

Several X-band SARs orbit the earth. Tasking these satellites through various entities provides SAR illuminators for which the collection geometry, the time of collection, and the possible signal power levels are known. SNL tasked two commercial, X-band SARs for the bistatic experiments conducted.

### **2.3.1 COSMO-SkyMed**

The X-band Italian SAR called COSMO-SkyMed (CSK) operates at 9.6 GHz center frequency, and a variable bandwidth from 180 to 400 MHz. It is funded by the Italian government ministry of defense, Ministero della Difesa (MDD) and ministry of education, universities, and research, Ministero dell'Istruzione, dell'Università, e della Ricerca, (MIUR), and operated by Agenzia Spaziale Italiana (ASI). Four CSK satellites are in low-earth orbit (LEO), sun-synchronous orbits at approximately 620 km above the earth, with an orbit inclination of  $97.9^\circ$  and an orbit cycle of almost 15 days. Together, the four satellites are able to repeat an image of a target within 24 hours. A typical image covers a 10 km by 10 km area.

### **2.3.2 TerraSAR-X**

TerraSAR-X (TSX) is a dual-use (commercial and military) X-band SAR with a 9.65 GHz center frequency operated by the public-private partnership between Deutsches Zentrum für Luft- und Raumfahrt (DLR) and Astrium/European Aeronautic Defence and Space Company (EADS). TSX is a single satellite in a LEO, sun-synchronous orbit of 514 km with an orbit inclination of  $97.4^\circ$  and an orbit repeat of 11 days. It has a maximum bandwidth of 300 MHz. A typical image covers a 5 km by 10 km area.

## **2.4 SAR Collections**

Six commercial SAR satellite images were tasked to coincide with deployment of the bistatic SAR ensemble both in New Mexico and in Nevada. These collections are shown in Table 1. SAR signals were captured for all collections except the August 15, 2013 TSX collection over SPE.

### 3. BISTATIC SAR IMAGERY

The bistatic SAR ensemble captures direct- and reflected- energy signals via the antennas with the same designations. The direct-energy channel provides the timing of the incoming energy in both channels. It also supplies characteristics of the impinging radio frequency (RF) radiation. This knowledge helps arrange the reflected energy into a phase history and provide the waveform to deconvolve the illuminating waveform and recover the target reflectivity. A two-line element (TLE) file provides the ephemeris for the SAR sensor. TLEs for most satellites are readily available on the internet. The process of estimating the waveform, data assembly, and image formation is covered in [2].

**Table 1: Table of commercial SAR collections for the field experiments.**

Satellite	Mode	Date and Time (UTC)	Azimuth Angle (degrees)	Look Angle (degrees)	Target
CSK-2	Enhanced Spotlight	11Jun13, 00:46:10	278.08	48.18	TAGC
CSK-3	Enhanced Spotlight	12Jun13, 00:46:16	278.08	48.19	TAGC
CSK-4	Enhanced Spotlight	15Jun13, 00:46:17	278.08	48.16	TAGC
TSX	High-Resolution Spotlight Mode	01Aug13 13:15:52	280.49	26.86	TAGC
TSX	High-Resolution Spotlight Mode	15Aug13 13:58:21	280.96	20.95	SPE
CSK-4	Enhanced Spotlight	16Aug13, 00:46:10	280.94	34.53	SPE

### 3.1 Image formation

For SAR imaging, the RADAR is side-looking from the platform and the RADAR illumination moves across the target as the SAR platform passes. In strip-map-mode SAR collections, the SAR's flight path drags the RADAR beam across a "strip" of the ground. In spotlight-mode SAR collections, the RADAR is steered to continually illuminate or "spotlight" the scene as the SAR platform passes. The steering can be accomplished electronically (an electronically-steered array (ESA)) or mechanically (a gimbal-mounted antenna) [3, 4]. CSX and TSX are strip-map-mode SARs with limited along-track, or azimuth, pointing capabilities utilizing their phased-array antenna designs [5]. Their azimuth-pointing capabilities allow a higher spatial resolution (in azimuth), pseudo-spotlight-mode collection.

A popular spot-light mode image formation algorithm is polar format algorithm (PFA) [3, 4, 6]. This algorithm will produce an image if the complex phase history is assembled coherently, and the ephemeris correctly predicts the satellite position during the collection.

### 3.2 Bistatic Images

Although Table 1 documents six collections, there were five bistatic collections captured during the proof-of-concept phase of this project. Four were captured at Kirtland AFB. Three of Kirtland bistatic data were illuminations by CSK; the other, TSX. Of the three CSK Kirtland collects, only June 10, 2013 will be presented. The fifth bistatic collection was a CSK at NNSS. The sixth was a TSX at NNSS. It was not collected as documented in [1].

#### 3.2.1 CSK: June 10, 2013

The polar format algorithm image of the June 10, 2013 CSK collected at 18:46:10 Mountain Daylight Time (MDT) is shown in Figure 6. This is a range-Doppler image with range being up and down the page. The bright spot at the top of the image is the position of the reflected-energy antenna. It is very bright due to targets reflecting close to the antenna, and possibly energy leaking in the back-lobe of the antenna. The bright lines emanating across the image and at a slight angle up and down the image from the reflected-energy antenna location are sidelobes from the point-spread function the antenna, a bright reflector.

The range resolution for monostatic and bistatic SAR collections is [4]

$$\rho_r = \frac{C}{2BW * \cos \theta}$$



where  $C$  is the speed of light, and  $BW$  is the bandwidth of the transmitted signal, and  $\theta$  is the depression angle of the central pulse of the collection. For the June 10, 2013 CSK collection, the range resolution is 0.843 m.

The back-scatter, bistatic cross-range resolution is given by [6]

$$\rho_{cr} = \frac{\lambda r_t r_r}{L_t r_r + L_r r_t} \quad 2$$

where

$$\lambda = \frac{C}{f_o} \quad 3$$

$f_o$  is the transmitted signal's center frequency,  $r_t$  is the range to the transmitter,  $r_r$  is the range to the receiver,  $L_t$  is the path or aperture traversed by the transmitter during signal transmission,  $L_r$  is the path traversed by the receiver during signal capture.  $L_r$  is zero for our experiment. For the June 10, 2013 CSK collection, the cross-range resolution is 1.487 m. Note that for a monostatic collection equation 2 becomes

$$\rho_{cr} = \frac{\lambda r^2}{L_t r + L_r r} = \frac{\lambda r}{2L} \quad 44$$

For the SNL ground-based bistatic SAR, a reduction in cross-range/Doppler resolution occurs because the bistatic receiver is stationary, reducing the bistatic aperture to half of the monostatic aperture swept out by CSK during the collection time or

$$\rho_{cr} = \frac{\lambda r_t^2}{L_t r_t} = \frac{\lambda r}{L} \quad 55$$

In Figure 6, a triangular area of illumination is apparent in the SAR image below the reflected-energy antenna's location with approximately a  $30^\circ$  angle, the field-of-view of the antenna. The targets closer to the reflected-energy antenna are brighter because of proximity to the antenna. The targets farther from the antenna exhibit energy decrease because the reflected power drops as the inverse of the target to antenna distance squared. The extent of the SAR image is approximately 8200 m from the antenna to far-range reconstructed targets.

Figure 7 shows a close-up of the TAGC from Figure 6. The trees, the fairways, and water hazards are apparent in the image. The Tijeras Arroyo is to the left of the golf course. Note that roads are not straight, but curved. PFA assumes that the returning wave is planar, which is true when the distance from the target to the receiver is very large. Yet, the range from the ground-based reflect-antenna to the target is comparatively small to the range to the LEO satellites. Therefore, the returning electro-magnetic waves not planar, but spherical with curved wavefronts as a function of range.

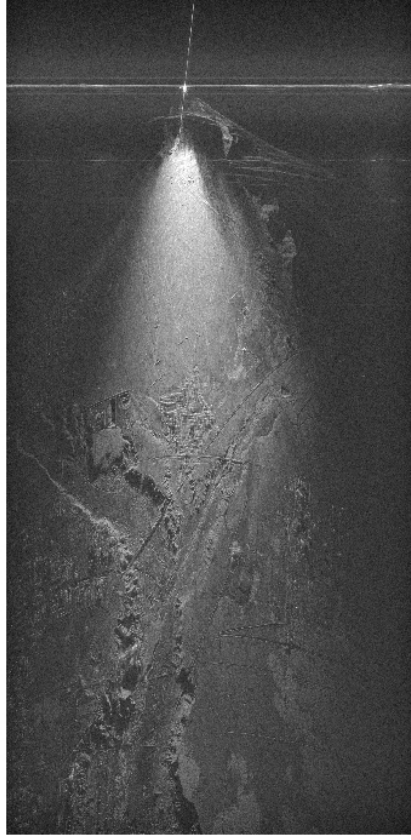


**Figure 6: Radar coordinates bistatic SAR image of the TAGC from Manzano Mountain on June 10, 2013, 18:46:10 MDT.**

Wavefront curvature manifests itself in two ways in the planar-wave assumption of PFA. First is a geometric distortion, the curved roads as example seen in Figure 7. Secondly is a defocussing of SAR targets farther from scene center [8]. The largest image radius that can be reconstructed without wavefront curvature defocus is [7]:

$$r_{\max} = \sqrt{2\lambda} \left( \frac{L_t^2}{r_t^3} + \frac{L_r^2}{r_r^3} \right)^{-1/2} \quad 6$$

where  $r_{\max}$  is the image radius,  $\lambda$  is the SAR wavelength,  $L_t$  and  $r_t$  are the same as defined above. For all of the SNL bistatic, equation 6 reduces to

$$r_{\max} = \sqrt{2\lambda} \left( \frac{L_t^2}{r_t^3} \right)^{-1/2} \quad 77$$

for  $L_r = 0$ . Defocussing because of wavefront curvature is not apparent in our bistatic imagery. This is consistent with equation 7 which yields a radius of 9259 m without defocus with the CSK collection parameters. The image in Figure 6 has a range dimension of 8200 m, or a radius of 4100 m if the image patch was circular, well within the focused patch size.

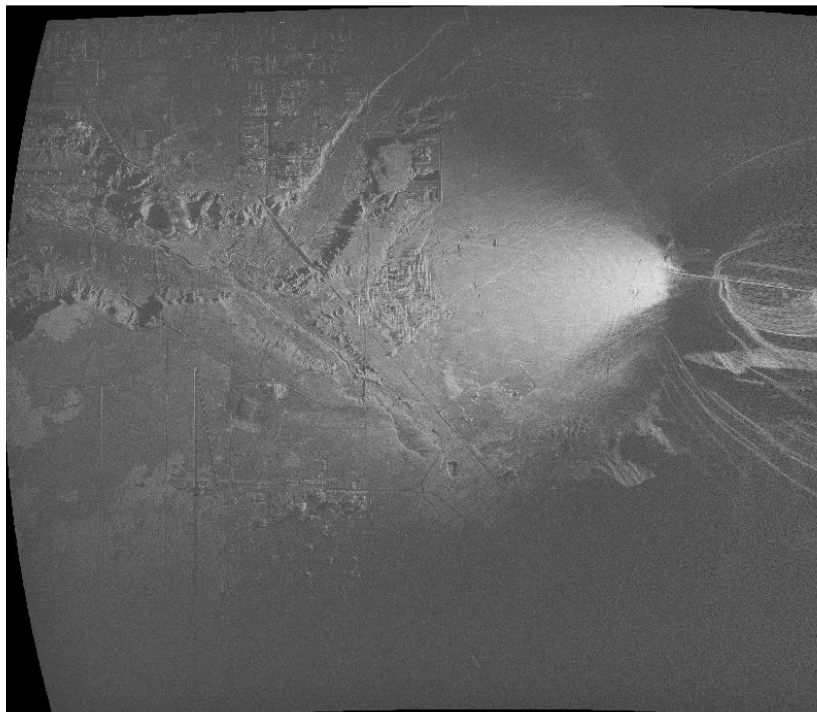
Figure 8 presents a geo-located image of the entire reconstructed bistatic CSK image. This geo-located data was put on a latitude/longitude grid [8]. Figure 9 shows a close-up of geo-located imagery of TAGC from CSK on June 10, 2013. The image on the left is the geo-located bistatic CSK imagery captured from Manzano Mountain. The image on the right is the geo-located monostatic CSK image. Note that the target reflectivity and shadows are quite different in the bistatic and monostatic images. The trees at the TAGC are smeared in the bistatic image and not in the monostatic image. Doppler smearing is a target defocus phase function resulting from either a velocity in Doppler or range [9]. Because there is no defocus in the monostatic image, the defocus is most likely due to movement in the range direction of the bistatic image which is along the bisector vector of the receive-energy antenna range with an elevation angle of  $5.6^\circ$  and the monostatic range vectors with an elevation angle of  $42.8^\circ$ . For June 10, 2013, the range vector has a bistatic elevation angle of  $24.2^\circ$ . Apparently, the tree canopies have more motion in the range direction at this shallow elevation angle versus the  $42.8^\circ$  monostatic elevation angle.

Figure 10 zooms in on the TAGC even more. Here, glints off of power lines that run parallel to the road are denoted. The power line catenary is perpendicular to the SAR collection geometry only at certain positions of the power lines, producing a strong, corner-type return. Also, the range-direction return-antenna sidelobe signal superimposes itself on the underlying terrain reflectors. The faint sidelobe energy is high-lighted between two red lines in Figure 10.





**Figure 7: Close-up of the TAGC. Note the roads are curved due to wavefront curvature using PFA.**



**Figure 8: Geo-located bistatic SAR image of TAGC captured on June 10, 2013. This image is on a latitude/longitude grid.**



**Figure 9: The image on the left is the bistatic SAR, geo-located image of TAGC. The image on the right is the monostatic CSK SAR image from the commercial imagery vender. Note the differences in shadows. The bistatic elevation angle is about  $5.6^\circ$  and the monostatic elevation is  $42.8^\circ$ , making the bistatic shadows more pronounced. The target reflectance are quite different in some cases.**

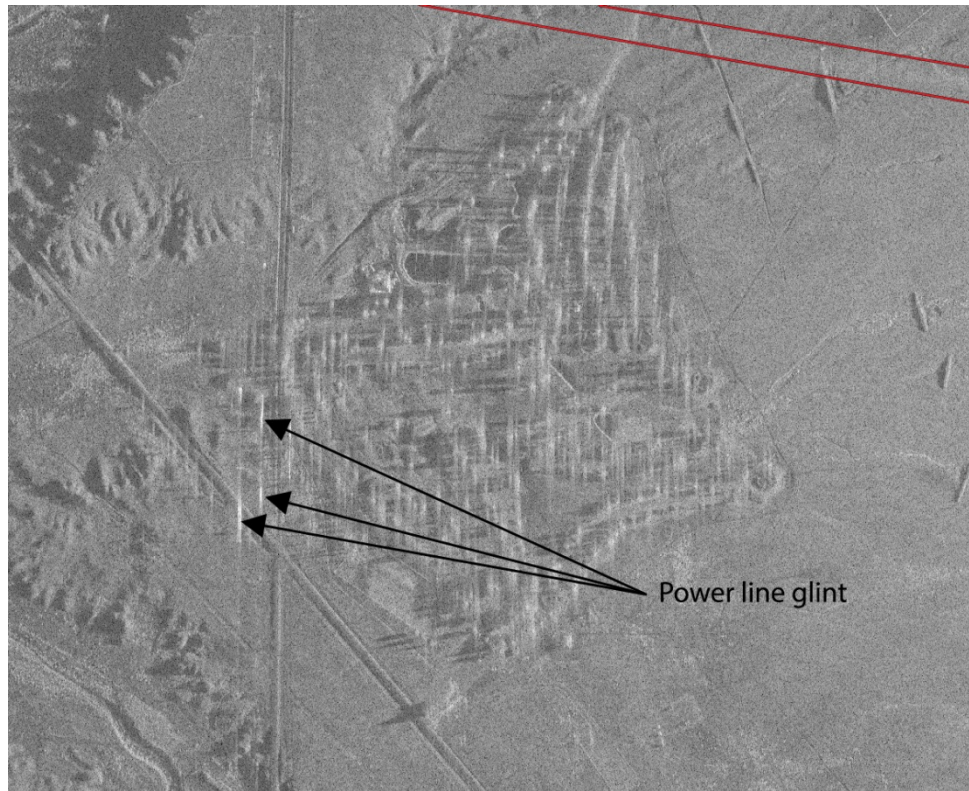


**Figure 10: Close-up of the CSK June 10, 2013 TAGC bistatic imagery. Here the glint off the power lines that exist along the golf course is seen as well as the faint return-energy antenna sidelobe inside the red lines. The tree canopy motion defocus because of wind is apparent.**

### 3.2.2 TSX: August 1, 2013

The polar format algorithm image of the August 1, 2013 TSX collected at 07:15:52 MDT is shown in Figure 11. This is a range-Doppler image with range being up and down the page. Overall, the image resembles the CSK images captured in June. The extent of the SAR image is approximately 9500 km from the antenna to far-range reconstructed targets. The TSX collection was pseudo-spot-light-mode. The range resolution is 0.708 meters and the cross-range resolution is 1.641 meters.

Figure 12 presents a geo-located, latitude/longitude grid image of the entire reconstructed bistatic TSX image. Figure 13 shows a close-up of geo-located imagery of TAGC from TSX on August 1, 2013. The image on the left is the geo-located bistatic TSX imagery captured from Manzano Mountain. The image on the right is the geo-located monostatic TSX image captured at the satellite. Note that the target reflectivity and shadows are quite different in the bistatic and monostatic images. Compared to the CSK bistatic imagery in Figure 9 and 10, the motion of the trees is negligible in the TSX bistatic image.

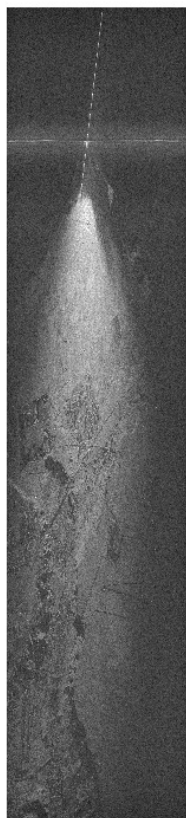


**Figure 11: TSX Bistatic image of TAGC captured on August 1, 2013, 07:15:52 MDT. Image created using PFA.**

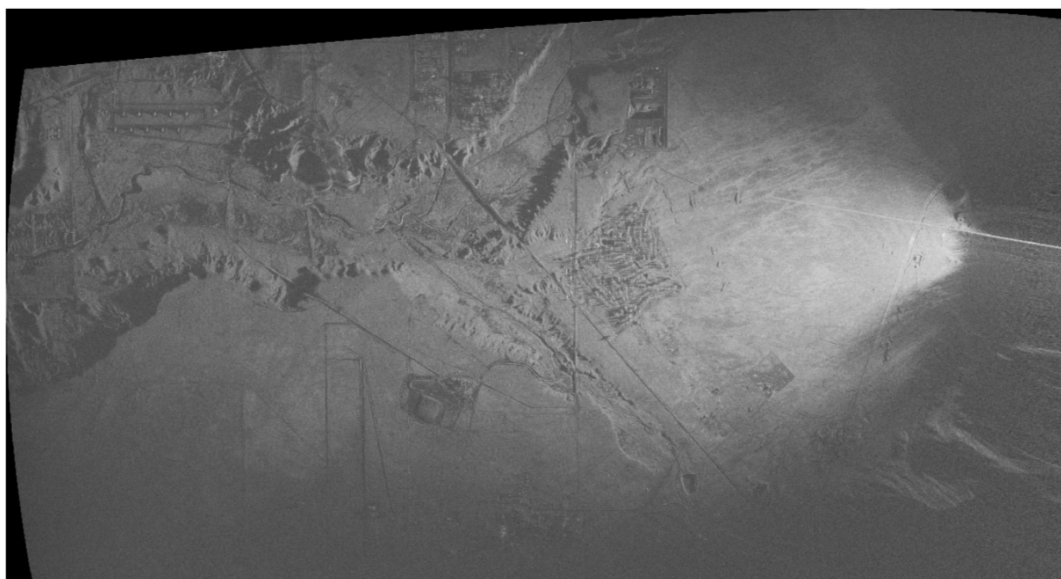


**Figure 12: Geo-located TSX bistatic SAR imagery captured August 1, 2013 from Manzano Mountain**



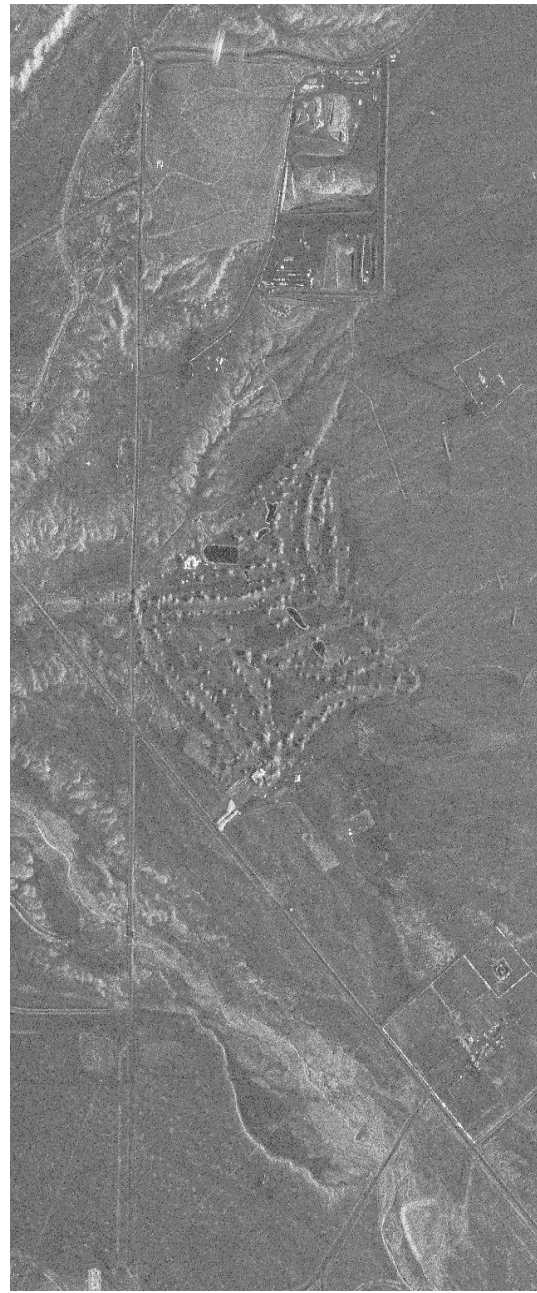
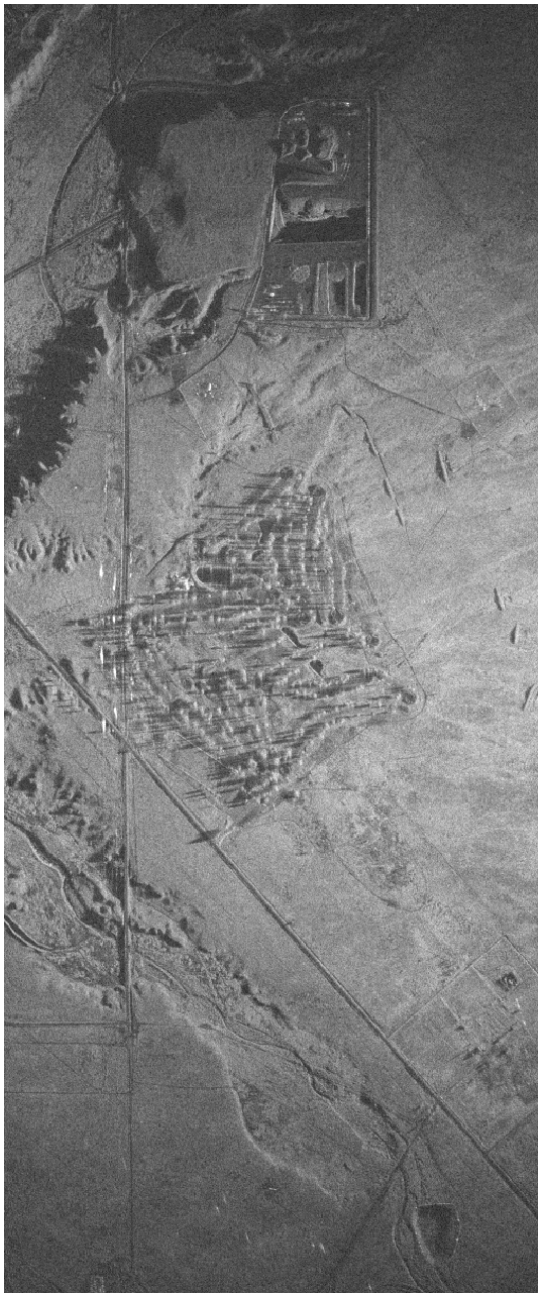


**Figure 13: The left image is a close up of TAGC from the geo-located bistatic TSX SAR imagery. The right image is a close up of TAGC from the geo-located monostatic TSX SAR image.**

### 3.2.3 CSK: *SPE Overlook, August 15, 2013*

The polar format algorithm image of the August 15, 2013 CSK collected at 18:46:10 PDT at NNSS SPE site is shown in Figure 14. This is a range-Doppler image with range being up and down the page. The extent of the SAR image is approximately 8600 km from the antenna to far-range reconstructed targets. The range resolution is 0.714 meters and the Doppler resolution is 2.872 meters. The Doppler/cross-range resolution is lower than the back-scatter geometry because the aperture angle subtended by the transmitter is projected along the bistatic bisector angle slant-plane, compressing the equivalent aperture traversed.

Figure 15 shows the geo-located CSK bistatic SAR imagery of the SPE site. The SPE site and the Sedan crater are annotated in this image. The reflected-energy antenna site has been cropped from the picture, but is just off the top right-most corner. Figure 16 presents a close-up of the SPE site's pad from the CSK August 15 collection. Note the large shadows in the bistatic image on the left due to the reflect-energy antenna's low elevation angle. The bistatic geometry makes the bistatic imagery appear quite different than the monostatic image. The shallower look angle for the monostatic image rids the imagery of many shadows, but introduces possible layover for most of the mountains around the SPE pad (see Figure 17 for a graphical representation of geometric distortions found in SAR imagery). The reflected energy off the pad for the monostatic image is less than the bistatic. Higher signal levels may make changes more noticeable on the pad using the bistatic imagery than using the monostatic imagery.

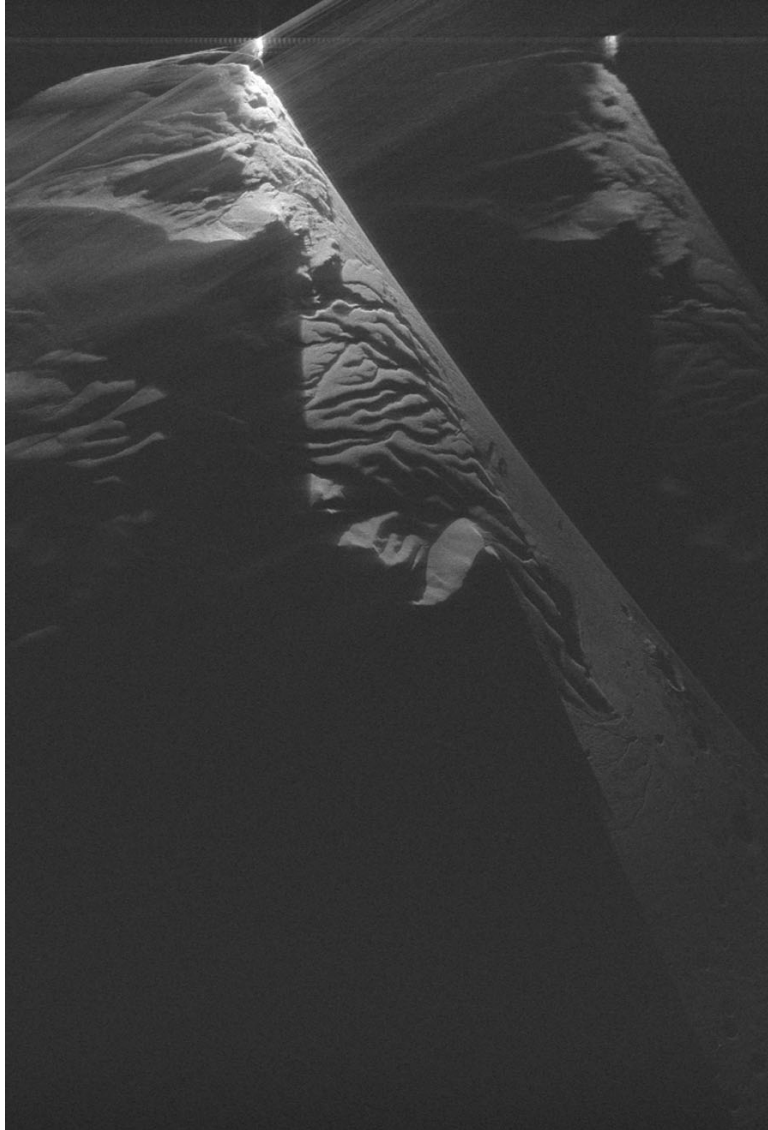


**Figure 14: Bistatic SAR image created using PFA of the SPE site and its surrounding area.**

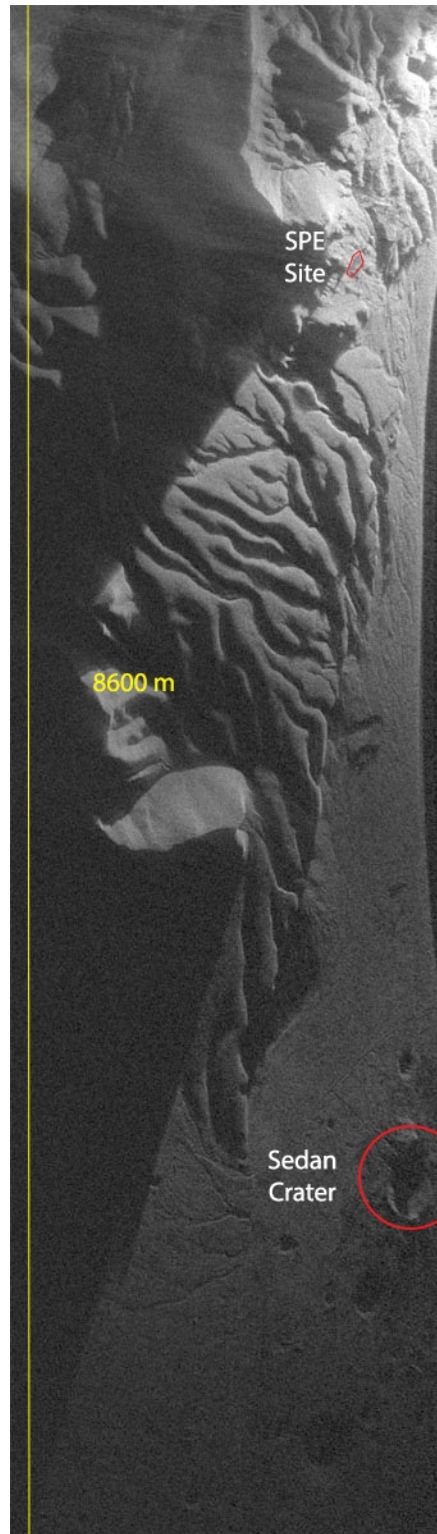


**Figure 15: Geo-located bistatic SAR image of the SPE site and its surroundings. The SPE site and Sedan crater are called-out in the image.**



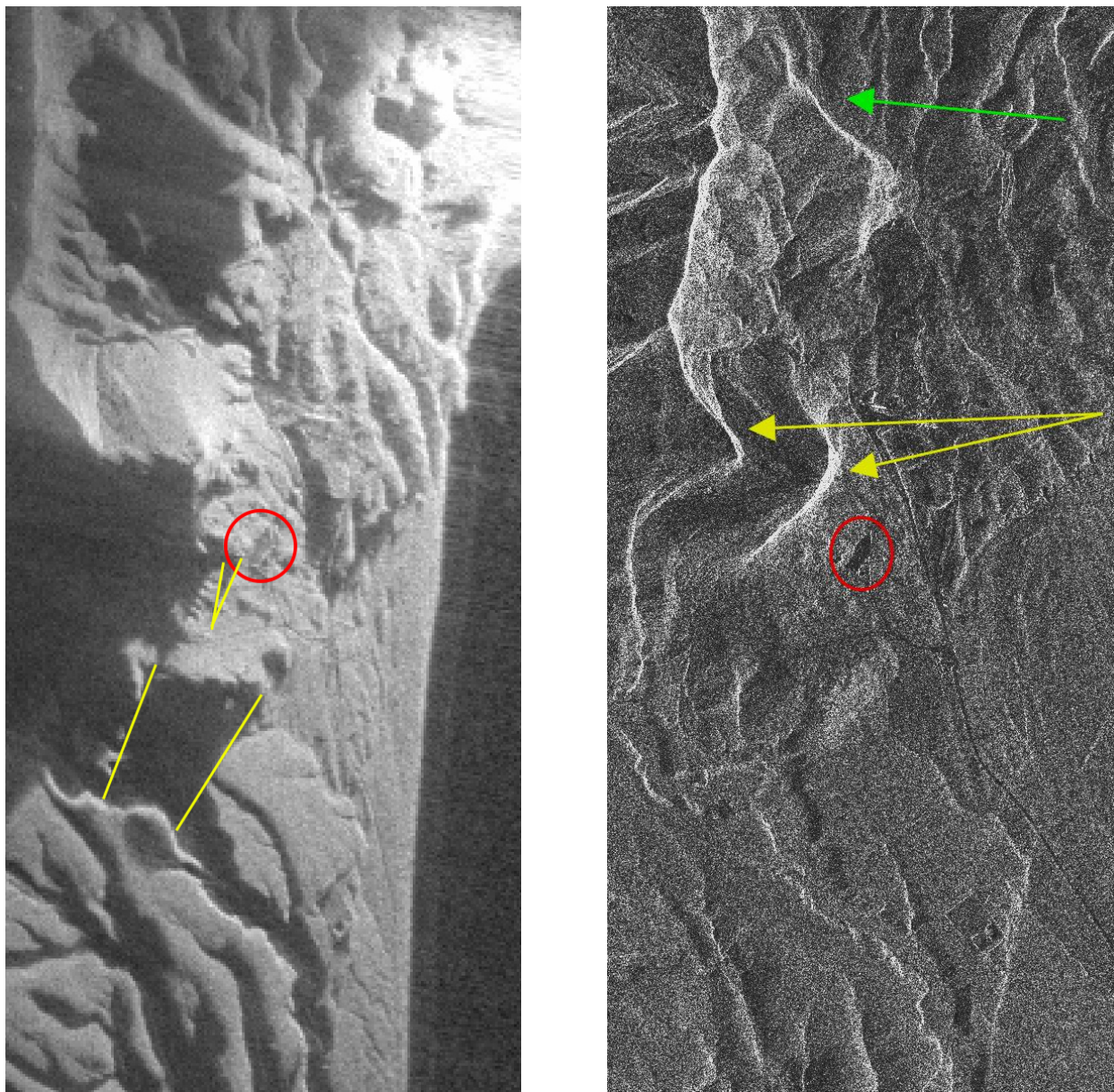


**Figure 16: The left image is the bistatic image formed from captured CSK signals on August 15, 2013 at 18:46:10 PDT of the SPE pad and surrounding area. The elevation angle of the reflect-energy antenna was  $5.5^\circ$ . The yellow lines delineate receiver shadows. The red circle encloses the SPE pad. The right image is the monostatic CSK image. The green arrow denotes the direction of illumination. The yellow arrows show possible areas of layover. The information about the mountain slopes here are virtually lost and distorted in the SAR range direction. The SPE pad and the road to it are darker in the monostatic than the bistatic image.**

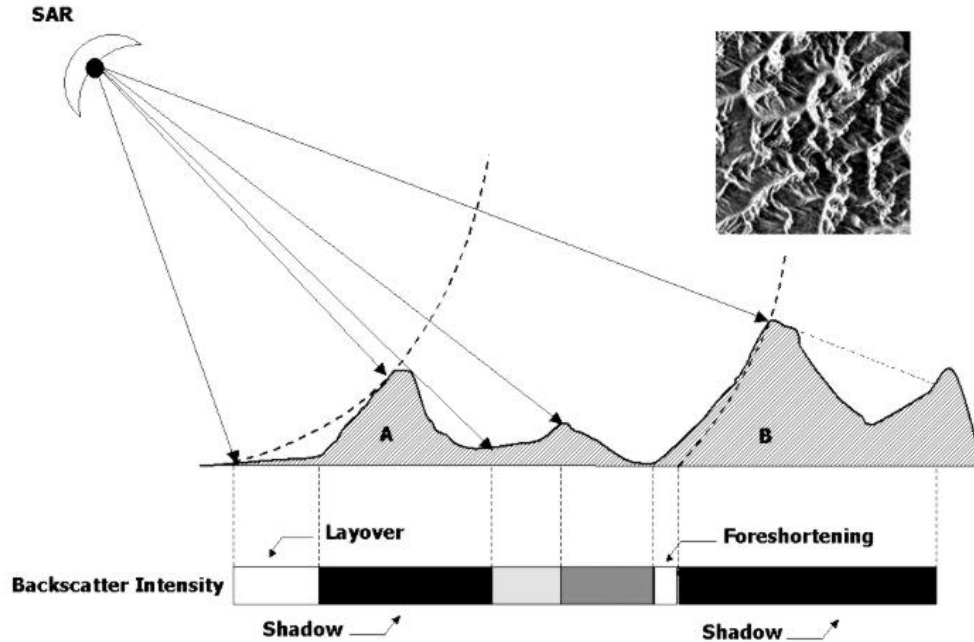


**Figure 17: Image distortions in SAR imagery. Layover occurs when a target of height, i.e., a mountain appears in the same range as a lower height target, i.e. a valley. Foreshortening occurs when sloped sides of a mountain are contracted in size because of slope and height of the mountain<sup>1</sup>.**

### 3.3 Image quality

As noted above, the SPE pad and its surroundings appear brighter in the bistatic imagery than in the monostatic imagery. A cursory investigation examining magnitude levels in the images can confirm or refute this perception.

Finding very dark shadows in the image, the noise level of the image can be measured. Areas of interest, like the SPE pad, can then be measured, using an average signal level over that image. The subsequent signal to noise (SNR) in decibels (dB) can be calculated using:

$$\text{SNR}_{\text{dB}} = 20\log_{10}\text{SNR} = 20\log_{10}\frac{S}{N} \quad 8$$

where  $S$  is the signal magnitude value, and  $N$  is the noise magnitude value. The SPE pad SNR in the monostatic image is 15.6 dB. The SNR value for the SPE pad in the bistatic image is 21.3 dB. Therefore, the signal of the SPE pad is about 4 times greater in the bistatic image. This is significant in monitoring change on the SPE pad. Such change products are presented in the next section.

<sup>1</sup> [http://www.geog.ucsb.edu/~jeff/115a/remote\\_sensing/radar/radar1.html](http://www.geog.ucsb.edu/~jeff/115a/remote_sensing/radar/radar1.html)



## 4. BISTATIC IMAGE PRODUCTS

SAR is an all-weather, day-night imagery which can be utilized in detecting temporal changes captured in the SAR imagery [11, 12]. The follow sections discuss two types of change detection. One is a magnitude change detection technique that balances and displays two collections as a color image. Changes in magnitude reflection show as changes in color in the composite image. The other is a coherent change detection that utilizes both magnitude and phase changes in a pair of complex-value images.

### 4.1 Two-Color Multi-View

SAR imagery, the magnitude detected output of the complex-valued image, can show temporal changes; magnitude changes due to changes in reflectance. A technique of displaying these magnitude changes consists of placing two images separated in time into a red-green-blue color image. The earliest, date and time-wise image is placed into the red band. The latest image is placed into the green and blue bands. Thus, two colors will be evident if there is magnitude change. Red will be present if the target is in the earliest image and not the latest, and cyan if the target is the latest image but not the earliest. The color key to remember for two-color multi-view (2CMV) is “Red fled; Blue new”, ignoring that blue is really cyan. If the two SAR image gray levels are matched on average, targets with no change will appear gray, much like a single magnitude SAR image.

Figure 18 shows the 2CMV of June 10, 2013 (red) and June 11, 2013 (green & blue) TAGC bistatic imagery. The overall background is grayish meaning there is no change. There are small vehicle differences in the TAGC parking lot and changes caused by glint off the power lines on the left of the image. Figure 19 shows the 2CMV of June 11, 2013 (red) and June 14, 2013 (green & blue) bistatic imagery. Here the intensity of June 11 is a little higher giving the overall reddish hue of the image. Notable changes are blue vehicles in the golf course parking lot, blue glint off the power lines, and three red vehicles “fled” near the right-middle of the image.

### 4.2 Coherent Change Detection

SAR is a coherent imaging sensor. The signals collected and processed are complex-valued, meaning they have both magnitude and phase. After signal processing and image formation, the final SAR imagery is also complex-valued, encoding the reflected target’s magnitude and phase. If several SAR collections closely repeat the same collection geometry, the complex-valued reflection between images should be approximately identical, and the complex correlation between the same target should be high. However, if the reflection is changed between collections, either by natural or human means, the complex correlation would be lower compared to the original measure. This change can be due to magnitude or phase reflectance change or a

combination of both magnitude and phase. The change measure between two coherent collections has been called interferometric change detection, or coherent change detection (CCD) [4, 11, 12, 13, 14].

Given two SAR collections that have almost identical collection geometries, the complex correlation between collections is

$$\mu = \frac{\left| \sum_{k=1}^N f_k^* g_k \right|}{\sqrt{\sum_{k=1}^N |f_k|^2 \sum_{k=1}^N |g_k|^2}} \quad 9$$

where  $f$  is the complex-valued reflectance from the earlier collection,  $g$  is the complex-valued reflectance from the later collection,  $k$  is the index of pixel values in the neighborhood box for the local estimation,  $N$  is the number of pixels in that estimation box,  $*$  denotes the complex-conjugate operator, and  $|\cdot|$  denotes the absolute-value operation. The complex correlation is also called the coherence [15].

This complex-correlation measure is an estimation, and uses a neighborhood of  $N$  complex image pixels to calculate the complex correlation or coherence of the portion of the image. Also, use of equation 8 assumes that the two complex-valued SAR images have been registered to less than a pixel offset. SNL performs registration using a multi-scale registration technique [16].

The three CSK collections over Kirtland AFB on June 10, June 11, and June 13, 2013, were coherent collections. Note in Table 1, the collection angles are almost identical. These angles are for the monostatic collections. The geometry of the resulting bistatic collection is the slant plane along the bisector vector between the transmitter and receiver slant planes. Bistatic angles for the collections are shown in Table 2.

Figure 20 shows the full-scene CCD between June 10 and June 11, 2013 CSK bistatic images. Bright pixels mean higher correlation. Dark pixels mean decorrelation. The complex correlation from equation 9 is directly related the signal-to-noise (SNR) level of the imagery by [17, 18]

$$\mu = \frac{1}{1 + \frac{1}{\text{SNR}}} \quad 10$$

The fall-off in complex correlation follows the beam roll-off or return signal in Figure 20.

Figure 21 shows a close up of the TAGC area with the bistatic imagery from June 10, 2013 and the CCD between June 10 and June 11, 2013. The moving trees decorrelated because the

reflectors are different between collections. The shadows decorrelated because of no/low signal return. The sidelobe from June 10, 2013 decorrelates because it is in a slightly different position on June 10 than on June 11. The road to the south and west of TAGC is paved, and has low signal return. Some roads off this main road are dirt, and could be decorrelated due to vehicle traffic between the June 10 and June 11 collections.

Given equation 10 and the increased signal on the SPE pad in the CSK August 15, 2013 bistatic collection, the CCD values on a correlated SPE pad in a bistatic CCD would be 0.92 versus 0.86 for the monostatic CCD. For a monostatic SNR of 1 at scene center, the bistatic CCD correlated level would be 0.80 while the monostatic CCD correlated level would be 0.50. The higher, bistatic correlation, in each case, provides greater sensitivity to CCD changes, if they are present.

**Table 2: Table of coherent CSK collections over Kirtland AFB with bistatic collection geometry angles.**

Satellite	Mode	Date and Time (UTC)	Azimuth Angle (degrees)	Look Angle (degrees)	Target
CSK-2	Enhanced Spotlight	11Jun13, 00:46:10	266.91	68.94	TAGC
CSK-3	Enhanced Spotlight	12Jun13, 00:46:16	267.13	68.95	TAGC
CSK-4	Enhanced Spotlight	15Jun13, 00:46:17	267.11	68.93	TAGC



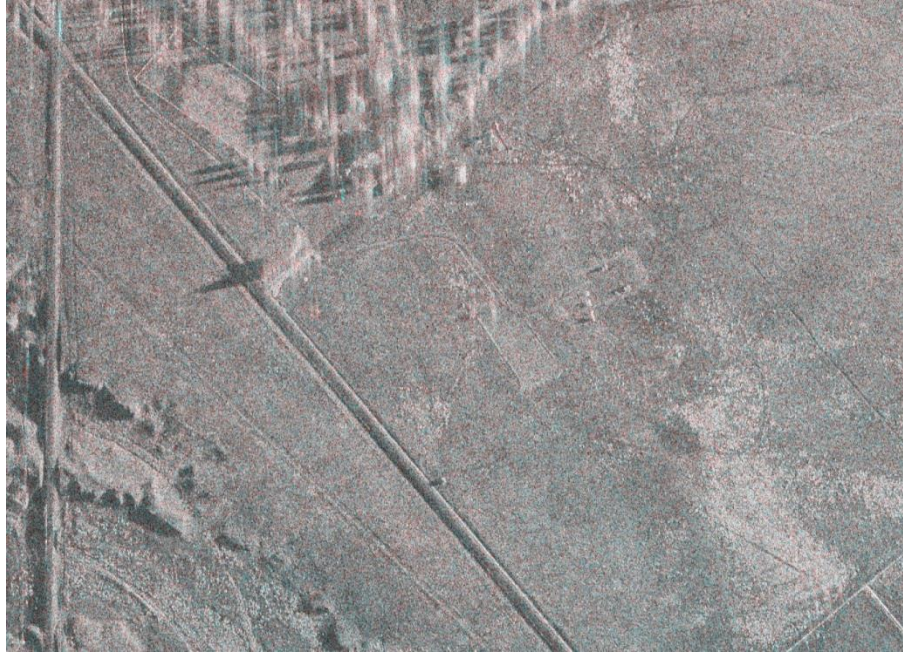


**Figure 18: Two-color multi-view (2CMV) of June 10, 2013 (red) and June 11, 2013 (green & blue) TAGC bistatic imagery. The overall background is grayish meaning there is no change. Yet there are small vehicle differences in the TAGC parking lot. There are changes of the glint off the power lines on the left of the image and tree structures at the top of the image.**

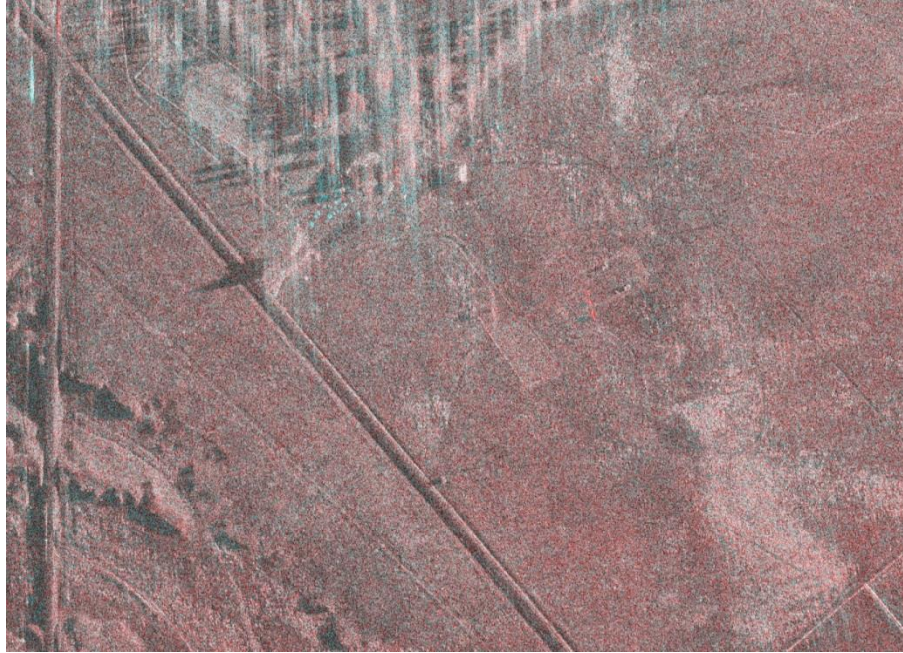


**Figure 19: The 2CMV of June 11, 2013 (red) and June 14, 2013 (green & blue) bistatic imagery at TAGC. Here the intensity of June 11 is a little higher giving the overall reddish hue of the image. Notable changes are blue vehicles in the golf course parking lot and blue glint off the power lines. Other changes include red and blue changes in the tree structure, and three vehicles “fled” near the right-middle of the image.**



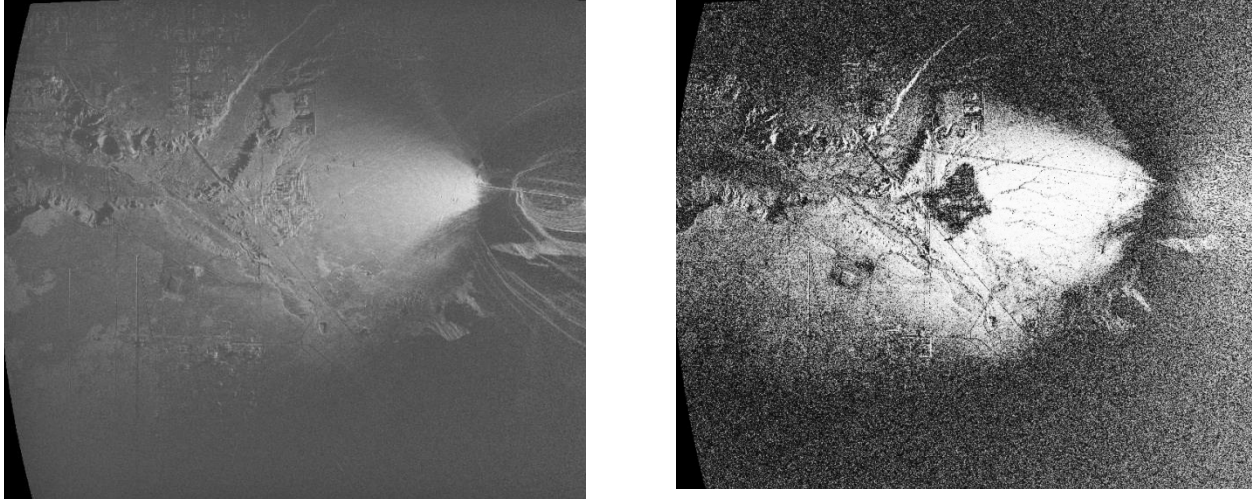


**Figure 20: The left-most figure is the CSK June 10, 2013 bistatic, geo-located image of TAGC. The right-most figure is the coherent change detection (CCD) of the CSK June 10, 2013 and June 11, 2013. White pixels are high-valued complex correlation. CCD is dependent on the two images signal-to-noise, so the targets closer to the receive-energy antenna on the right-side of both images, can be higher correlated if no temporal change has occurred between collected images. Also, targets farther from the receive antenna will have inherently lower signal-to-noise, thus lower complex correlation/CCD value.**

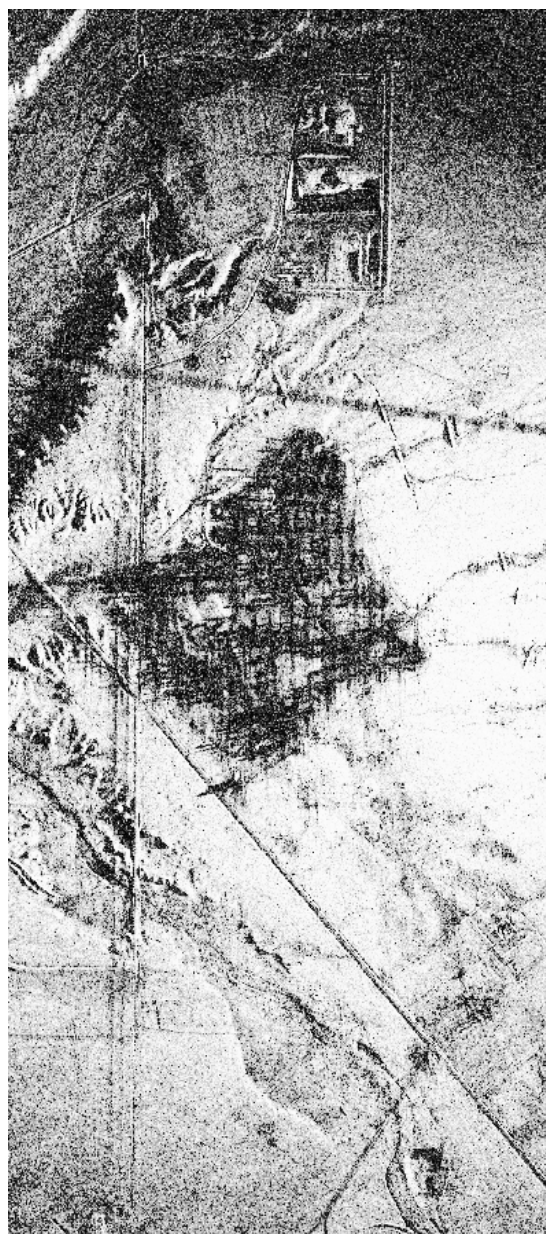


**Figure 21: The left-most image is a close-up of the TAGC area of June 10, 2013 CSK bistatic imagery. The right-most image is the CCD between June 10, 2013 and June 11, 2013. Note the smeared tree canopies in the image also show as decorrelation (low values) in the CCD. The sidelobe that is barely visible in the image decorrelates in the CCD. Areas of low returns such as shadows are also decorrelated in the CCD.**

[This page intentionally blank]

## **5. CONCLUSIONS**

SNL developed the means to capture spaceborne SAR signals using a ground-based system. Images from the digitized and formatted signals were accomplished using the polar format

algorithm. For Kirtland AFB, the bistatic SAR imagery was collected in a backscatter geometry. The imagery experiences wavefront curvature geometric distortion which leads to curved linear objects and a keystone-like distortion. Distortion correction is demonstrated by geo-locating the imagery. Wind-induced defocus can appear in bistatic imagery even though it is not apparent in the monostatic imagery because the equivalent bistatic collection geometry can exhibit a different sensitivity to motion than the monostatic collection geometry.

The NNSS collection produced a bistatic SAR image that is a side-scattering geometry. The imagery produces an area which no range-Doppler coordinates from the bistatic geometry intersect the earth, producing a line of demarcation between imagery and void. The SNR from the monostatic imagery versus the bistatic imagery shows a 4-times increase in the signal power from the SPE pad in the bistatic imagery compared to the monostatic imagery.

Two types of change detection were demonstrated using three Kirtland AFB CSK collections. 2CMV can be produced if the resulting imagery can be registered and the mean gray-level values balanced. CCD can be produced using the bistatic SAR collection if the transmitters repeat their collection geometries and a pair of SAR images are coherent with respect to each other. The increased SNR a bistatic image can lead to higher CCD correlation and higher sensitivity to complex-valued changes between imagery.

## REFERENCES

- [1] D. A. Yocky, N. E. Doren, T. A. Bacon, D. E. Wahl, P. H. Eichel, C. V. Jakowatz Jr, G. G. Delaplain, D. F. Dubbert, B. L. Tise and K. R. White, "Bistatic SAR: Proof of Concept," Sandia National Laboratories: National Center for Nuclear Security Report, Albuquerque, 2013.
- [2] D. E. Wahl and D. A. Yocky, "Bistatic SAR: Processing Description," Sandia National Laboratories: National Center for Nuclear Security Report, Albuquerque, 2013.
- [3] W. G. Carrara, R. S. Goodman and R. M. Majewski, *Spotlight Synthetic Aperture Radar: Signal Processing Algorithms*, Boston: Artech House, Inc., 1995.
- [4] C. V. Jakowatz Jr., D. E. Wahl, P. H. Eichel, D. C. Ghiglia and P. A. Thompson, *Spotlight-mode Synthetic Aperture Radar: A Signal Processing Approach*, Boston: Kluwer Academic Publishers, 1996.
- [5] P. Capece, "Active SAR antennas: Design, development and current programs," *International Journal of Antennas and Propagation*, vol. 2009, no. Article ID 796064, p. 1-11, 2009.
- [6] P. H. Eichel, "IFP 4.0: A polar-reformatting image formation processor for synthetic

- aperture radar," Sandia National Laboratories: 2005-5232, Albuquerque, 2005.
- [7] B. D. Rigling and R. L. Moses, "Polar format algorithm for bistatic SAR," *IEEE Transactions on Aerospace and Electronic Systems*, vol. 40, no. 4, pp. 1147-1159, 2004.
  - [8] N. E. Doren, C. V. Jakowatz Jr, D. E. Wahl and P. A. Thompson, "General formulation for wavefront curvature correction in polar-formatted spotlight-mode SAR images using space-variant post-filtering," in *Proceedings of the IEEE International Conference on Image Processing*, Santa Barbara, 1997.
  - [9] P. H. Eichel, "Fast algorithms for 3-D terrain mapping using spotlight-mode SAR stereo," in *Proceedings for the Workshop on Synthetic Aperture Radar Technology*, Huntsville, 2002.
  - [10] J. R. Fienup, "Detecting moving targets in SAR imagery by focusing," *IEEE Transactions on Aerospace and Electronic Systems*, vol. 37, no. 3, pp. 794-809, 2001.
  - [11] J. Villasenor and H. A. Zebker, "Studies of temporal change using RADAR interferometry," in *SPIE conference on Synthetic Aperture Radar*, Los Angeles, 1992.
  - [12] D. A. Yocky and B. F. Johnson, "Repeat-pass dual-antenna synthetic aperture radar interferometric change detection post processing," *Photogrammetric Engineering and Remote Sensing*, vol. 64, no. 5, pp. 425-429, 1998.
  - [13] D. A. Yocky and C. V. Jakowatz Jr, "Two-height effects on interferometric synthetic aperture radar coherence," in *Proceeds of the SPIE: Algorithms for Synthetic Aperture RADAR Imagery VII*, Orlando, 2000.
  - [14] M. A. Preiss, D. A. Gray and N. J. S. Stacy, "Detecting scene changes using synthetic aperture radar interferometry," *IEEE Transactions on Geoscience and Remote Sensing*, vol. 44, no. 8, pp. 2041-2054, 2006.
  - [15] R. Touzi, A. Lopes, J. Bruniquel and P. W. Vachon, "Coherence estimation for SAR imagery," *IEEE Transactions on Geoscience and Remote Sensing*, vol. 37, no. 1, pp. 135-149, 1999.
  - [16] P. H. Eichel, "MREG V1.1: A multi-scale image registration algorithm for SAR applications," Sandia National Laboratories: SAND2013-6567, Albuquerque, 2013.
  - [17] E. Rodriguez and J. M. Martin, "Theory and design of interferometric synthetic aperture radars," *IEE Proceedings-F*, vol. 139, no. 2, pp. 147-159, 1992.
  - [18] D. L. Bickel and W. H. Hensley, "Design, theory, and applications of interferometric synthetic aperture radar for topographic mapping," Sandia National Laboratories: SAND96-1092, Albuquerque, 1996.

## DISTRIBUTION

1		Veraun Chipman NCNS/CIT Program Manager National Security Technologies (NSTec) PO Box 98521 M/S NLV101 Las Vegas, NV 89193-8521	
1	MS0971	Robert M. Huelskamp	5750
1	MS1207	Terry A. Bacon	5962
1	MS1207	Neall E. Doren	5962
1	MS1207	Charles V. Jakowatz, Jr.	5962
1	MS1207	Daniel E. Wahl	5962
4	MS1207	David A. Yocky	5962
1	MS1209	John E. Gronager	5960
1	MS0899	Technical Library	9536 (electronic copy)





